14th International Symposium on Turbulence and Shear Flow Phenomena (TSFP14)
Heidelberg, Germany, July 28–31, 2026

ACOUSTIC ROSSITER MODES WITH VARYING SPAN WIDTHS IN TRANSONIC CAVITY FLOWS WITH INCOMING TURBULENT BOUNDARY LAYERS

Yuto Fujimoto
Department of Aerospace Engineering, Graduate School of Engineering
Tohoku University
6-6-01, Aramaki Aza Aoba, Aoba-ku, Sendai, Miyagi, 980-8579, Japan
yuto.fujimoto@dc.tohoku.ac.jp

Soshi Kawai
Department of Aerospace Engineering, Graduate School of Engineering
Tohoku University
6-6-01, Aramaki Aza Aoba, Aoba-ku, Sendai, Miyagi, 980-8579, Japan
kawai@tohoku.ac.jp

ABSTRACT

The effects of the spanwise extent and incoming boundary-layer thickness on resonant tones in a Mach 0.6 cavity flow with an incoming turbulent boundary layer were investigated using implicit large-eddy simulations. Flow over an open cavity can generate self-sustained oscillations and discrete cavity tones, which are major sources of aerodynamic noise in practical systems. However, limited knowledge is available regarding the modal amplitudes and unsteady behavior of these tones. To clarify these issues, the spanwise width-to-depth ratio, W/D, and the incoming boundary-layer thickness ratio, δ_0/D, were varied. The results show that the behavior of each Rossiter mode depends on both the spanwise extent and the boundary-layer thickness, and that their effects differ from mode to mode. Statistically, the pressure amplitude of the first Rossiter mode decreases as the spanwise width increases, which is attributed to the breakdown of spanwise-coherent vortical structures. In addition, temporal mode switching between three Rossiter modes was observed for the first time, and the dominant mode was found to correspond to the number of instantaneous coherent vortical structures. These findings demonstrate that the spanwise extent and incoming boundary-layer thickness jointly govern both the modal amplitudes and the unsteady behavior of resonant tones in cavity flows.

INTRODUCTION

Open cavity flow is governed by a wide range of parameters, including geometric parameters such as L/D and W/D, where L and W denote the cavity length and spanwise width, respectively, as well as flow parameters such as the Reynolds number, Mach number, and boundary-layer properties, and it remains challenging to clarify how these diverse parameters affect the cavity tones. For the frequencies of cavity tones, a predictive formula has been established through Rossiter's pioneering study (Rossiter (1964)) and its subsequent compressibility correction (Heller *et al.* (1971)), as shown in the following equation.

$$St_{L,n} = \frac{f_n L}{U_\infty} = \frac{n-\alpha}{\left[M_\infty\left(1+\frac{\gamma-1}{2}M_\infty\right)^{-\frac{1}{2}}+\frac{1}{\kappa}\right]} \tag{1}$$

In this equation, n denotes the nth Rossiter mode, γ is the ratio of specific heats, κ is the convection-velocity constant ($= 0.57$) defined by $U_c = \kappa U_\infty$, and α is the phase lag ($= 0.25$). These cavity tones are encountered in practical applications, including aircraft landing-gear, and their reduction is desired.

In laminar cavity flows, the effects of the Reynolds number, Mach number, and L/D have been investigated in considerable detail using bi-global instability analysis (Sun *et al.* (2017)). By contrast, for turbulent cavity flows, which are of greater practical relevance, previous studies have mainly focused on the cavity length-to-depth (L/D) ratio and Mach number (M_∞) (Lawson & Barakos (2011); Beresh *et al.* (2016)), which are central parameters in Rossiter-type discussions, whereas the effects of other parameters have received comparatively less attention. Although the incoming boundary layer has long been recognized as affecting the amplitude of cavity tones (Rossiter (1964); Ahuja & Mendoza (1995)), it remains unclear how this effect depends on the individual Rossiter modes.

The current understanding of the mechanism underlying cavity tones can be summarized as follows. The interaction between downstream-convecting shear-layer disturbances and upstream-propagating acoustic waves establishes a fluid–acoustic feedback loop that generates large-scale vortical structures (Yokoyama & Kato (2009)) and organizes the resonant pressure field into spatially ordered, nearly spanwise-coherent modal structures (Casper *et al.* (2018)). From the viewpoint of flow control, it has been shown that, although suction and blowing at the cavity leading edge have long been known to suppress cavity tones (Rowley & Williams (2006)), recent studies have demonstrated that unsteady spanwise-distributed actuation is also effective (Liu *et al.* (2021)). This

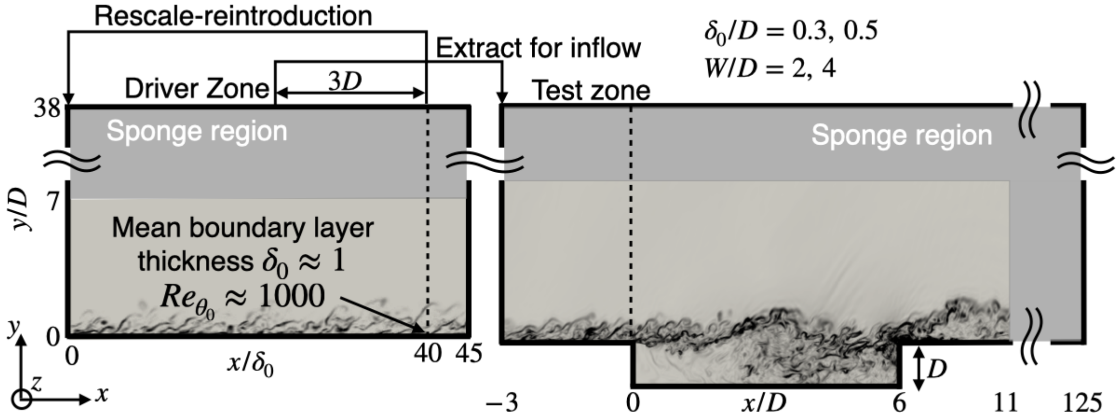

Figure 1. Computational schematics and parameters of this study

finding motivates a detailed examination of spanwise effects in cavity-tone dynamics. Furthermore, three-dimensionality is also known to arise during the transition between laminar and turbulent states, as reported by Picella *et al.* (2018).

Moreover, a salient feature is mode switching, in which the dominant Rossiter mode varies in time; Kegerise *et al.* (2004) reported its first experimental observation. However, its underlying mechanism remains unclear, and elucidating the physical mechanism is important.

This study focuses on cavity tonal noise at a freestream Mach number of $M_\infty = 0.6$ and aims to elucidate how the dominant Rossiter mode and its unsteady behavior depend on the spanwise extent of the computational domain W. We performed implicit large-eddy simulations (ILES) at momentum thickness Reynolds number $Re_{\theta_0=1000}$ with $\delta_0/D = (0.3, 0.5)$ for spanwise extents W/D = (2,4).

METHODOLOGY

In this study, we conduct implicit large-eddy simulations using an in-house code, which has been extensively verified. The spatial derivative is evaluated by the sixth-order compact scheme (Lele (1992)) with an eighth-order compact low-pass filter (Lele (1992); Gaitonde & Visbal (1999)) where the filter coefficient is set to 0.48. The time integration uses the third-order TVD Runge–Kutta Scheme (Gottlieb & Shu (1998)). Figure 1 shows the schematic of the cavity flow simulation. The computational domain is partitioned into two zones: the driver zone and the test zone. The driver zone was used to create the turbulent boundary layer using the rescaling-reintroduction inflow method (Urbin & Knight (2001)). The turbulent boundary layer was generated such that the Reynolds number based on the momentum thickness satisfies Re_{θ_0}=1000. Here, the subscript 0 denotes time-averaged quantities evaluated in the driver zone at the streamwise station that, after convection, coincides with the cavity leading edge dashed line in Figure 1. The free stream Mach number is set to $M_\infty = 0.6$. We performed simulations by varying the spanwise width-to-depth ratio as $W/D = 2$ and 4, and the incoming boundary-layer thickness-to-depth ratio as $\delta_0/D = 0.3$ and 0.5. In all cases, the streamwise length of the driver zone was fixed at $L_x = 22.5D$ ($45\delta_0$) to preclude low-frequency contamination (Simens *et al.* (2009); Morgan *et al.* (2011)). All other reference lengths were scaled by the cavity depth D. The test zone included a cavity of size $(L_x, L_y, L_z) = (6D, D, W)$. The domain sizes were $(22.5D, 38D, W)$ for the driver zone and $(128D, 38D, W)$ for the over-cavity region of the test zone, where W denotes the spanwise extent. For the case of

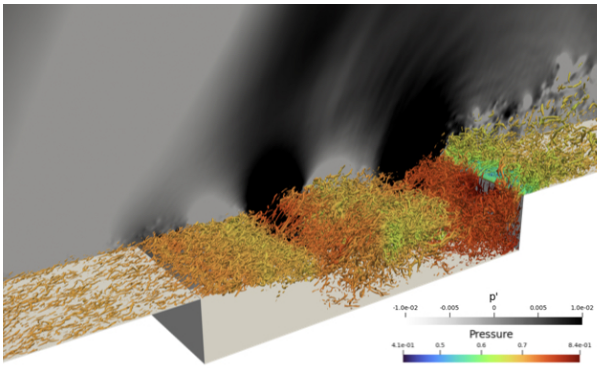

Figure 2. Iso-surfaces of the Q-criterion at $Q/(U_\infty/\delta_0)^2 = 1.5$, colored by static pressure p, with the background colored by pressure fluctuations p', for the case of $\delta_0/D = 0.3$ and $W/D = 2$.

$W/D = 2, \delta_0/D = 0.3$, the number of grid points is approximately 46 million in the driver zone and 72 million in the test zone. For cases with a larger spanwise extent, the number of grid points scales as a constant multiple of that in the $W/D = 2$ case.

The grid spacing normalized by viscous length in each direction, $\Delta x^+, \Delta y_w^+, \Delta z^+$ is set to 20, 0.8, 10 in the driver zone and the test zone. In the streamwise and wall-normal directions, the grid is stretched, whereas a uniform grid is employed in the spanwise direction. The streamwise spacing is varied such that $\Delta x^+ \approx 3$ at the cavity leading edge and $\Delta x^+ \approx 0.8$ near the trailing edge. Within the cavity, the grid spacings are bounded by $\Delta x^+ \leq 20$ and $\Delta y^+ \leq 20$. A sponge region was added to prevent acoustic reflections at the computational boundary (Mani (2012)). Periodic boundary conditions were imposed in the spanwise direction.

RESULTS

Overview of cavity flow

Figure 2 shows iso-surfaces of the second invariant of the instantaneous velocity-gradient tensor (Q-criterion) representing vortical structures for the case of $W/D = 2$ and $\delta_0/D = 0.3$. The vortical structures are colored by static pressure, and the background shows the instantaneous distribution of pressure fluctuations. As seen in figure 2, the turbulent boundary layer flows into the cavity region, and the shear layer develops as it convects downstream. The vortical structures become increasingly three-dimensional toward the trail-

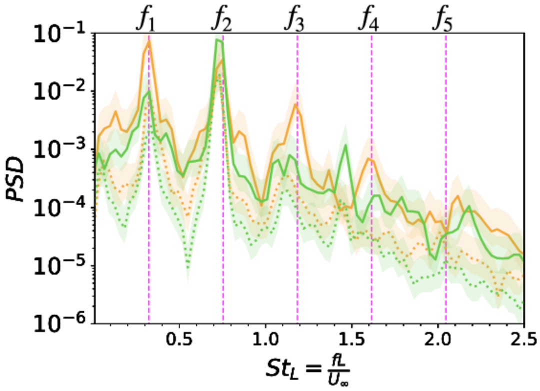

Figure 3. Span-averaged power spectral density (PSD) of pressure fluctuations at the cavity trailing edge ($x/D = 6, y/D = -0.05$). The magenta vertical lines indicate the Rossiter-mode frequencies predicted by Eq. (1). Green and orange lines denote $W/D = 4$ and $W/D = 2$, respectively. Solid and dashed lines correspond to $\delta_0/D = 0.3$ and 0.5, respectively.

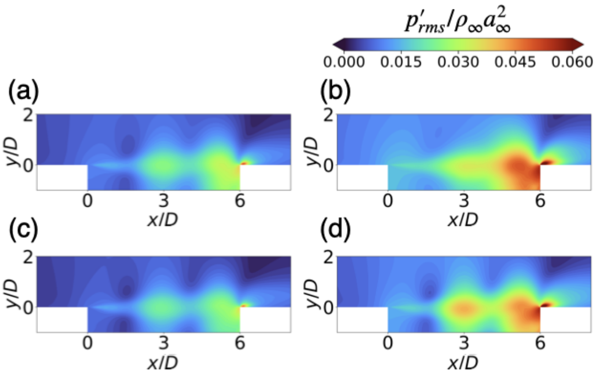

Figure 4. Root-mean-square pressure fluctuation (a) $W/D = 2, \delta_0/D = 0.5$ (b) $W/D = 2, \delta_0/D = 0.3$ (c) $W/D = 4, \delta_0/D = 0.5$ (d) $W/D = 4, \delta_0/D = 0.3$

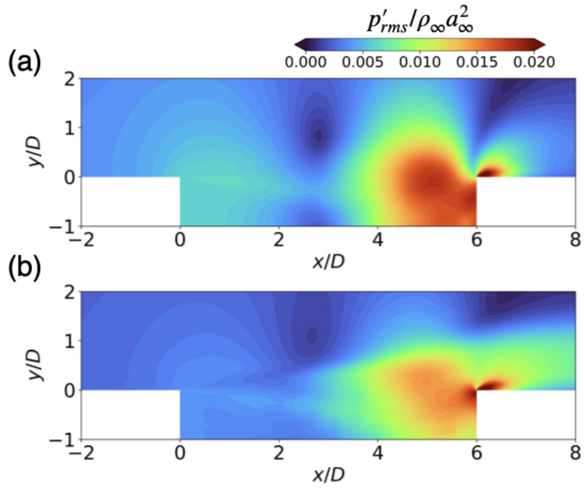

Figure 5. Band-pass-filtered pressure fluctuations at first Rossiter mode for $\delta_0/D = 0.3$: (a) $W/D = 2$, (b) $W/D = 4$.

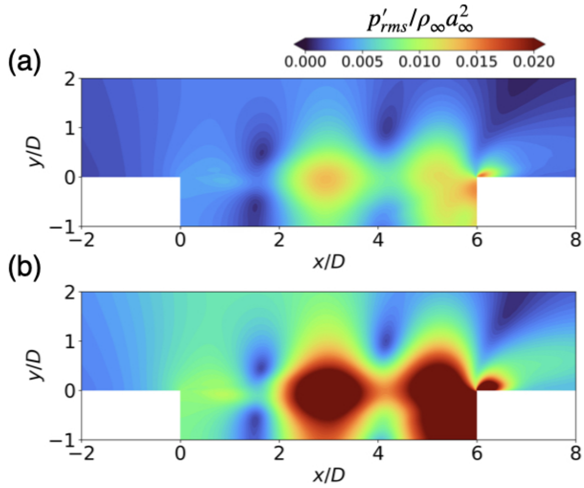

Figure 6. Band-pass-filtered pressure fluctuations at second Rossiter mode for $\delta_0/D = 0.3$: (a) $W/D = 2$, (b) $W/D = 4$.

ing edge. In this instantaneous field, a locally high-pressure region is also observed near the cavity trailing edge. The background pressure-fluctuation field further indicates the presence of two wavelengths of pressure fluctuations across the cavity in the streamwise direction, which are considered to be associated with the large-scale vortical structures. In addition, resonant acoustic waves radiated above from the vicinity of the cavity trailing edge can be identified.

Statistical characteristics

To assess the presence of resonant tones, the PSD of the span-averaged wall-pressure fluctuation along the spanwise line on the rear wall at $(x, y) = (6D, -0.05D)$ is shown in figure 3. Here, the line color denotes the spanwise domain width, while the line style indicates the incoming boundary-layer thickness. The PSD was estimated using Welch's method applied to the span-averaged signal, with blocks containing ten periods of the first Rossiter mode, 50% overlap, and averaging over nine segments. The error bars represent the 95% confidence intervals estimated from the chi-squared distribution. The magenta vertical lines represent the Rossiter frequencies given by Eq. (1). From the lowest to the highest frequency, these correspond to the first through fifth Rossiter modes ($St_L = 0.32, 0.75, 1.18, 1.62$, and 2.05). Figure 3 shows that, when cases with the same spanwise width (same color) are compared, the case with the thinner incoming boundary layer (solid line) exhibits a larger PSD over the entire frequency range. In contrast, when the effect of spanwise width is examined for a fixed incoming boundary-layer thickness (same line style), the PSD at the first Rossiter mode decreases as the spanwise width increases (green), irrespective of the boundary-layer thickness. Furthermore, when focusing on the frequency band with the largest peak amplitude, only the case with $W/D = 2$ and $\delta_0/D = 0.3$ is dominated by the first Rossiter mode, whereas the other cases are dominated by the second Rossiter mode.

To examine the spatial extent of the acoustic field, figure 4 shows the span-averaged p'_{rms}. Since the difference appears more clearly for $\delta_0/D = 0.3$, the following discussion focuses on this case. Similar to the dominant modes identified in the PSD, the case in (b) ($W/D = 2$ and $\delta_0/D = 0.3$) exhibits a qualitatively different trend from the other cases. In (b), a dominant pressure-fluctuation region, which is considered to be associated with the first Rossiter mode, is observed over $x/D = 4$–6. In contrast, in the other cases, pressure-fluctuation regions attributed to the second Rossiter mode are observed.

To confirm this interpretation, the RMS fields obtained by applying band-pass filters over $St_L = [0.18, 0.5]$ and $[0.5, 1.0]$ are shown in figures 5 and 6, respectively. Figures 5 and 6 show standing-wave-like pressure fluctuation distributions with one and two wavelengths, respectively. However, as pointed out by Casper *et al.* (2018), these distributions may also be interpreted as the envelope of the net travelling waves, as discussed in more detail in the next subsection. In terms of the amplitude, a comparison of the two figures shows a trend consistent with that observed in figure 3 at the first Rossiter mode; the magnitude of the pressure fluctuations is larger in the case of $W/D = 2$, whereas at the second Rossiter mode, the case of $W/D = 4$ exhibits a larger fluctuation level over most of the spatial domain.

As discussed above, the dominant Rossiter mode was found to depend on the spanwise extent not only in the spectral sense but also in its spatial distribution. To examine how each Rossiter mode is distributed in the spanwise direction, figure 7 shows instantaneous pressure fields on spanwise planes at $y/D = -0.5$, band-pass filtered at the Rossiter-mode frequencies for the cases with $\delta_0/D = 0.3$. A comparison of the first Rossiter mode between panels (a) and (c) shows a clear difference in the spanwise organization of the pressure structures. In the narrow-span case, $W/D = 2$ (a), a spanwise-coherent pressure structure is clearly observed, whereas in the wider-span case, $W/D = 4$ (c), this structure becomes disrupted. By contrast, for the second Rossiter mode, both panels (b) and (d) exhibit pressure structures that remain coherent in the spanwise direction. These results suggest that, for the first Rossiter mode, increasing the spanwise extent leads to a breakdown of the spanwise-coherent structure, thereby reducing the PSD level.

To further quantify this tendency statistically, figure 8 compares the results obtained by reversing the order of spanwise averaging and PSD estimation. The dash-dotted lines denote the spectra obtained by first computing the PSD and then performing spanwise averaging, whereas the solid lines represent those obtained by first spanwise averaging the pressure signal and then computing the PSD. For most cases, the Rossiter peaks have nearly the same amplitude irrespective of the order of these operations, suggesting that the underlying structures are coherent across the span. In contrast, for the first Rossiter mode in the $W/D = 4$ case, the PSD obtained by first computing the spectrum and then taking the spanwise average is larger than that obtained in the reverse order. This indicates that, when the spanwise average is taken first, cancellation occurs because of the spanwise variation of the pressure field. Therefore, the first Rossiter mode is suggested to lose its spanwise coherence as the spanwise computational extent increases, which in turn leads to a reduction in the PSD level.

Unsteady characteristics

To clarify the unsteady behavior of the Rossiter modes, figure 9 shows the time–frequency maps obtained by wavelet transforms of the pressure data at a location $(6D, -0.05D)$ upstream of the rear wall. Here, the horizontal magenta dashed lines indicate the Rossiter frequencies predicted by Eq. (1). First, all cases exhibit intermittent behavior, in which the modal intensity becomes stronger and weaker over time. It is also found that, for the narrow-span cases ($W/D = 2$), the behavior changes markedly depending on the incoming boundary-layer thickness. Defining mode switching as a change in the dominant mode over time, the case with the thinner incoming boundary layer, $\delta_0/D = 0.3$, is shown to exhibit switching among three modes, namely the first, second, and

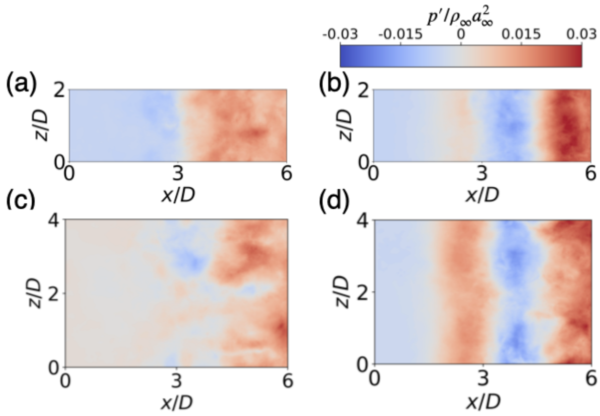

Figure 7. Instantaneous pressure fields on the spanwise plane at $y/D = -0.5$, band-pass filtered at the Rossiter-mode frequencies for the cases with $\delta_0/D = 0.3$: (a) first Rossiter mode, $W/D = 2$; (b) second Rossiter mode, $W/D = 2$; (c) first Rossiter mode, $W/D = 4$; and (d) second Rossiter mode, $W/D = 4$.

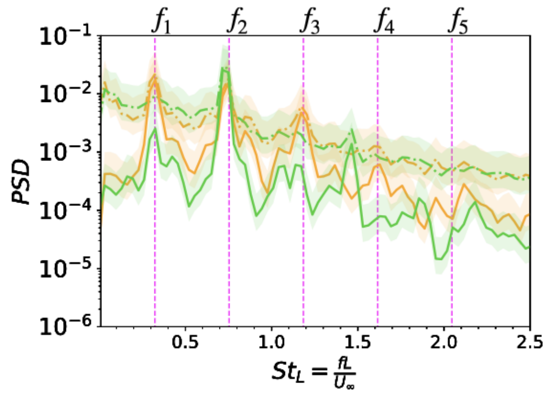

Figure 8. Power spectral density (PSD) of pressure fluctuations at the cavity trailing edge $(x/D = 6, y/D = -0.05)$ for $\delta_0/D = 0.3$. The magenta vertical lines represent the Rossiter frequencies predicted by Eq. (1). Green and orange lines correspond to $W/D = 4$ and $W/D = 2$, respectively. Solid lines denote the PSD estimated from the span-averaged signal, whereas dash-dotted lines denote the span-averaged PSD.

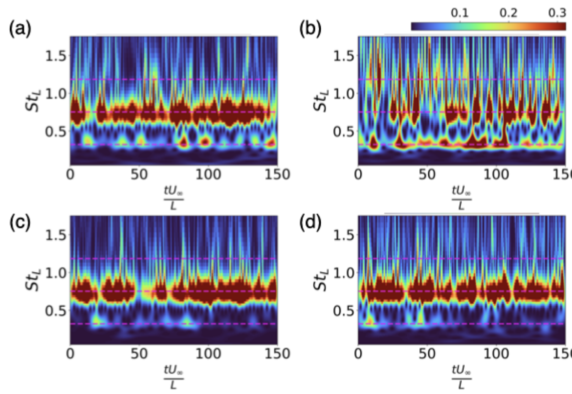

Figure 9. Time–frequency map obtained by wavelet transform at the cavity trailing edge$(x/D = 6, y/D = -0.05)$(a) $W/D = 2, \delta_0/D = 0.5$ (b) $W/D = 2, \delta_0/D = 0.3$ (c) $W/D = 4, \delta_0/D = 0.5$ (d) $W/D = 4, \delta_0/D = 0.3$.

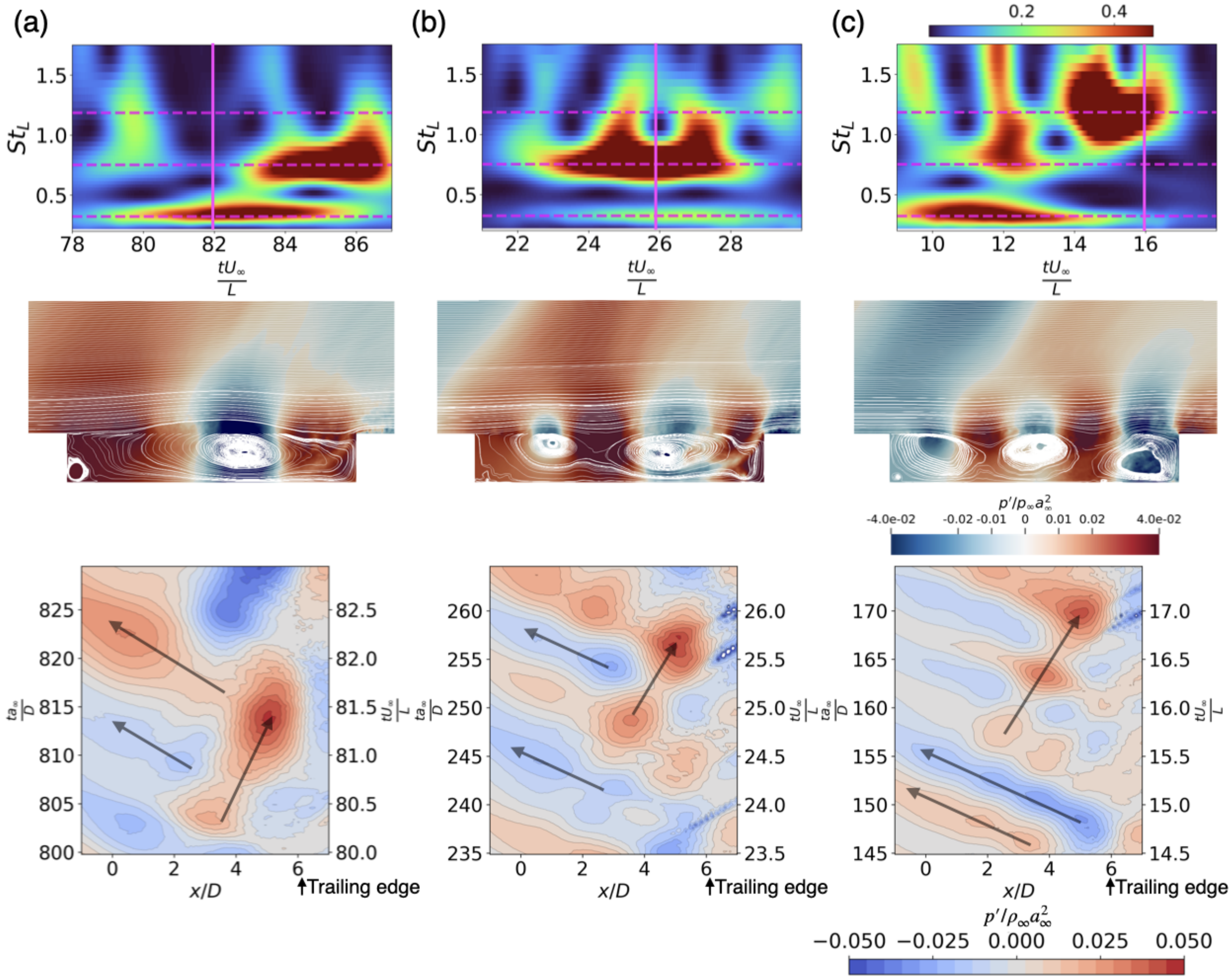

Figure 10. (a) First Rossiter mode dominant, (b) second Rossiter mode dominant, and (c) third Rossiter mode dominant time instants. Top row: Time–frequency maps obtained by wavelet analysis, while the horizontal magenta dashed lines indicate the Rossiter frequencies predicted by Eq. (1). Middle row: span-averaged instantaneous fields at the times indicated by the vertical solid magenta lines in the top row, colored by pressure fluctuation, with streamlines computed from the velocity field overlaid. Bottom row: *x*–*t* diagrams of the pressure fluctuations at y/D=6.

third Rossiter modes. In contrast, the case with the thicker incoming boundary layer, $\delta_0/D = 0.5$, exhibits mode switching between the first and second modes. On the other hand, in both wide-span cases ($W/D = 4$), the second mode remains dominant throughout the time series, and no mode switching is observed. These results indicate that mode switching is governed by the combined effects of the spanwise computational extent and the incoming boundary-layer thickness, rather than by either parameter independently.

To further clarify the characteristics of the $W/D = 2$, $\delta_0/D = 0.3$ case, which exhibits switching among three Rossiter modes, Figure 10 presents snapshots extracted at instants when each mode is dominant. (a), (b), (c) correspond to the first, second, and third Rossiter modes, respectively. For each panel, the top row indicates the corresponding interval in the time–frequency map obtained by wavelet transform, the middle row shows the span-averaged instantaneous field with streamlines computed from the velocity field and colored by pressure fluctuation, and the bottom row presents the *x*–*t* diagram of the pressure fluctuations at $y/D = 6$. Focusing on the streamlines in the middle row, it is found that the number of vortices identified by the streamlines corresponds to the Rossiter mode number. In addition, examination of the pressure fluctuations shows that negative pressure fluctuations are located at the vortex cores. These observations indicate that the dominant Rossiter mode corresponds closely to the span-averaged instantaneous vortical structure. This interpretation is also consistent with the standing-wave-like pressure patterns observed in the band-pass-filtered fields shown in figures 5 and 6. In these figures, the Rossiter modes appear as one-, two-, and three-wavelength standing-wave-like structures in the pressure field. Similarly, in the span-averaged instantaneous fields, the number of pressure wavelengths across the cavity is found to correspond to the dominant Rossiter mode number. Therefore, it is clarified that the structures shown in figure 4 represent the dominant Rossiter mode in each case. However, these instantaneous pressure structures are not fixed in space, unlike a true standing wave. Instead, the corresponding *x*–*t* diagrams indicate that they are net travelling waves propagating downstream, as evidenced by the pressure patterns extending from the lower left to the upper right, as indicated by the black arrows in figure 10. This interpretation is consistent with the argument of Casper *et al.* (2018), who suggested that, although time-averaged pressure fields exhibit standing-wave-like structures, the instantaneous dynamics are governed by net travelling waves whose envelope appears standing-wave-like after temporal averaging. Furthermore, the wavelength of the pressure fluctuations decreases from the first to the third Rossiter mode, in accordance with the change in the dominant large-scale vortical structures. At the same time, the *x–t* diagrams reveal both convective pressure disturbances propagating downstream and resonant acoustic waves emitted from the large-scale vortical structures and propagating upstream. These results demonstrate that the dominant Rossiter mode is closely linked not only to the large-scale vortical structures but also to the wavelength of the resonant acoustic waves generated by them.

CONCLUDING REMARKS

In this study, implicit large-eddy simulations were performed to investigate the amplitude and unsteady behavior of tonal noise in cavity flow by varying the spanwise width and the incoming boundary-layer thickness. The results showed that, for the first Rossiter mode, the PSD decreases as the spanwise width increases because the spanwise-coherent pressure structures are disrupted. In contrast, for the second Rossiter mode, the case with the wider span and thinner incoming boundary layer exhibits the most dominant spectral peak. These results indicate that the combination of spanwise width and incoming boundary-layer thickness leads to different behaviors depending on the Rossiter mode.

To examine the unsteady behavior, a wavelet analysis was further conducted, and, to the best of our knowledge, the case with $W/D = 2$ and $\delta_0/D = 0.3$ is the first in which switching among three Rossiter modes has been observed. For $\delta_0/D = 0.5$ and $W/D = 2$, switching between two modes was observed, whereas no mode switching was observed for $W/D = 4$. The result also demonstrates that the unsteady behavior depends on the combination of spanwise width and incoming boundary-layer thickness. Furthermore, in order to clarify the mechanism of the three-mode switching, representative instances at which each mode is dominant were extracted. The spanwise-averaged pressure and vortical structures showed that the Rossiter mode number corresponds to the number of vortices, and that negative pressure fluctuations are located at the vortex cores. In addition, *x–t* diagrams revealed that these large-scale pressure structures are propagating waves traveling downstream and are also closely related to the resonant acoustic waves. These findings demonstrate that the behavior of Rossiter resonance is governed, both statistically and unsteadily, by the combined effects of the spanwise width and the incoming boundary-layer thickness.

ACKNOWLEDGEMENTS

This work was supported in part by Japan Society for the Promotion of Science KAKENHI Grant Number 26H02169. Computer resources of the Fugaku supercomputer were provided by the RIKEN Advanced Institute for Computational Science through the HPCI System Research project (project ID hp240083, hp250090, hp260108). The authors would like to thank Soju Maejima for fruitful discussions.

REFERENCES

Ahuja, K.K. & Mendoza, J. 1995 Effects of cavity dimensions, boundary layer, and temperature on cavity noise with emphasis on benchmark data to validate computational aeroacoustic codes. *Tech. Rep.*.

Beresh, S.J., Wagner, J. L. & Casper, K. M. 2016 Compressibility effects in the shear layer over a rectangular cavity. *Journal of Fluid Mechanics* **808**, 116–152.

Casper, K. M., Wagner, J. L., Beresh, S. J., Spillers, R. W., Henfling, J. F. & Lawrence, Dechant J. 2018 Spatial distribution of pressure resonance in compressible cavity flow. *Journal of Fluid Mechanics* **848**, 660–675.

Gaitonde, D. & Visbal, M. 1999 Further development of a navier-stokes solution procedure based on higher-order formulas. In *37th Aerospace Sciences Meeting and Exhibit*, p. 557.

Gottlieb, S. & Shu, C. W. 1998 Total variation diminishing runge-kutta schemes. *Mathematics of computation* **67** (221), 73–85.

Heller, H., Holmes, D. G. & Covert, E. E. 1971 Flow-induced pressure oscillations in shallow cavities. *Journal of Sound and Vibration* **18** (4), 545–553.

Kegerise, M.A., Spina, E.F., Garg, S. & III, L.N. Cattafesta 2004 Mode-switching and nonlinear effects in compressible flow over a cavity. *Physics of Fluids* **16** (3), 678–687.

Lawson, S.J. & Barakos, G. N. 2011 Review of numerical simulations for high-speed, turbulent cavity flows. *Progress in Aerospace Sciences* **47** (3), 186–216.

Lele, S. K. 1992 Compact finite difference schemes with spectral-like resolution. *Journal of Computational Physics* **103** (1), 16–42.

Liu, Q., Sun, Y., Yeh, C., Ukeiley, L. S., CattafestaIII, L. N., Louis, N. & Taira, K. 2021 Unsteady control of supersonic turbulent cavity flow based on resolvent analysis. *Journal of Fluid Mechanics* **925**, A5.

Mani, A. 2012 Analysis and optimization of numerical sponge layers as a nonreflective boundary treatment. *Journal of Computational Physics* **231** (2), 704–716.

Morgan, B., Larsson, J., Kawai, S. & Lele, S.K. 2011 Improving low-frequency characteristics of recycling/rescaling inflow turbulence generation. *AIAA Journal* **49** (3), 582–597.

Picella, F., Loiseau, J-Ch, Lusseyran, F., Robinet, J-Ch, Cherubini, S. & Pastur, L. 2018 Successive bifurcations in a fully three-dimensional open cavity flow. *Journal of Fluid Mechanics* **844**, 855–877.

Rossiter, J. E. 1964 Wind-tunnel experiments on the flow over rectangular cavities at subsonic and transonic speeds. *Report No. 3438, Aeronautical Research Council* .

Rowley, C. W. & Williams, D. R. 2006 Dynamics and control of high-reynolds-number flow over open cavities. *Annu. Rev. Fluid Mech.* **38** (1), 251–276.

Simens, M. P., Jiménez, J., Hoyas, S. & Mizuno, Y. 2009 A high-resolution code for turbulent boundary layers. *Journal of Computational Physics* **228** (11), 4218–4231.

Sun, Y., Taira, K., CattafestaIII, L. N. & Ukeiley, L.S. 2017 Biglobal instabilities of compressible open-cavity flows. *Journal of Fluid Mechanics* **826**, 270–301.

Urbin, G. & Knight, D. 2001 Large-eddy simulation of a supersonic boundary layer using an unstructured grid. *AIAA Journal* **39** (7), 1288–1295.

Yokoyama, H. & Kato, C. 2009 Fluid-acoustic interactions in self-sustained oscillations in turbulent cavity flows. i. fluid-dynamic oscillations. *Physics of Fluids* **21** (10).